Additive Manufacturing Letters 10 (2024) 100216

Contents lists available at ScienceDirect

Additive Manufacturing Letters

journal homepage: www.elsevier.com/locate/addlet

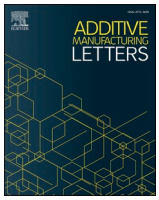

Short Communication

Additive manufacturing of NiTi architected metamaterials

C.A. Biffi [a], C. Soyarslan [b], J. Fiocchi [a], C. Bregoli [a], A. du Plessis [c], A. Tuissi [a], M. Mehrpouya [b,*]

[a] CNR ICMATE, National Research Council, Institute of Condensed Matter Chemistry and Technologies for Energy, Unit of Lecco, CNR ICMATE; Via Previati 1/e, 23900 Lecco, Italy
[b] Faculty of Engineering Technology, University of Twente, P.O. Box 217, 7500 AE Enschede, the Netherlands
[c] Comet Technologies Canada Inc, 460 Sainte-Catherine W, Montreal (Québec) H3B 1A7, Canada

ARTICLE INFO

Keywords:
Shape memory alloys
Functional performance
Architected metamaterials
Additive manufacturing
Laser Powder Bed Fusion

ABSTRACT

Additive manufacturing has revolutionized the creation of complex and intrinsic structures, offering tailored designs for enhanced product performance across various applications. Architected cellular or lattice structures exemplify this innovation, customizable for specific mechanical or functional requirements, boasting advantages such as reduced mass, heightened load-bearing capabilities, and superior energy absorption. Nonetheless, their single-use limitation arises from plastic deformation resulting from localized yield damage or plastic buckling. Incorporating NiTi shape memory alloys (SMAs) presents a solution, enabling structures to recover their original shape post-unloading. In this study, an NiTi architected metastructure, featuring auxetic behavior and a negative Poisson's ratio, was designed and fabricated via laser powder bed fusion (LPBF). The samples exhibit promising superelastic performance with recoverable deformation strains at room temperature. Comprehensive characterization processes evaluated the functional performance of the fabricated metastructures. The metastructure geometry promoted microstructure formation primarily along the wall thickness. Cycling compression tests, conducted at three applied force levels, demonstrated stable cyclic behavior with up to 3.8 % reversible deformation strain, devoid of plastic buckling or yielding damage. Furthermore, the NiTi metastructures displayed robust energy absorption capacity and damping behavior, underscoring their potential for reusable energy dissipators in various industries including aerospace, automotive, construction, and etc.

1. Introduction

Shape memory alloys (SMAs) belong to the category of smart materials with a unique capability to recover their original shape after deformation [1]. This thermally reversible shape recovery is a result of the phase transformation from low temperature (martensite) to high temperature (austenite), which is known as the shape memory effect (SME). Additionally, the superelasticity (SE) phenomenon is observed in the austenite phase (high-temperature) when mechanically stressed alloys have the ability to restore their original shape [2,3]. The SE properties hold promising potential for applications in energy and vibration damping, as they occur during phase transformations in loading-unloading cycles [4,5].

Additive manufacturing (AM) has brought about a revolution in the fabrication of complex-shaped structures, offering a unique solution for designers. Numerous studies have demonstrated the benefits of the laser powder bed fusion (LPBF) method in producing architected cellular structures with precise and diverse geometries, enabling designers to fine-tune tailored functional performance [6–8]. These structures possess a remarkable ability to dissipate or absorb kinetic energy from external mechanical loads in a controlled manner [9–13]. Nonetheless, a challenge encountered with architected metallic structures is the occurrence of unrecoverable deformation caused by inelastic buckling. However, the integration of SMAs provides an attractive alternative as it allows for recoverable deformation and exhibits energy dissipation characteristics through the SE effect. This, in turn, opens up exciting possibilities for designing and fabricating a wide range of energy absorption systems and structures with recoverable performance [14].

There are only a limited number of studies that explore the functional performance of SMA architecture structures. The difficulty lies in printing SMAs to achieve the desired functionality, as even slight changes in alloy composition or process parameters can significantly impact the transformation temperature and, subsequently, the thermomechanical performance of the printed structures [15,16]. In one study, Khademzadeh tackled this challenge by utilizing a small spot laser with low energy density [17]. This approach aimed to enhance the

* Corresponding author.
E-mail address: m.mehrpouya@utwente.nl (M. Mehrpouya).

https://doi.org/10.1016/j.addlet.2024.100216
Received 11 February 2024; Received in revised form 20 April 2024; Accepted 22 April 2024
Available online 23 April 2024

precision of the LPBF process when fabricating NiTi lattice structures, reducing the deviation of the printed lattices from the designed model. In another study, Gustmann et al. focused on investigating the impact of scanning strategy on the quality and mechanical properties of NiTi lattice structures [18]. The research demonstrated that the functional performance of these lattices can be precisely tailored by adapting the scanning vectors in the local area. Biffi et al. similarly highlighted the impact of scanning strategy on the print quality and functional performance of the lattices [19]. In their research, NiTi lattices showed partially superelastic properties during the compression test at room temperature, and the residual deformation was effectively recovered after the heating process above the temperature of 80°C.

Such smart structures hold promising potential for biomedical applications, such as bone implants, due to their elastic modulus and hysteretic behavior during stress cycling, which are similar to natural bone [20]. Following this idea, Adnani et al. investigated the shape memory performance and mechanical response of NiTi lattice structures fabricated by the LPBF technique [21]. They considered five levels of lattice porosity ranging from 32 % to 69 %. The study demonstrated that it is possible to decrease the elastic modulus of the lattices up to 86 % by enhancing the porosity level while maintaining the shape memory performance of the NiTi lattices. In another study, Dadbakhsh et al. also showed that the shape and geometry of the unit cells in NiTi lattice structures directly impact the shape memory response, and these factors can be controlled and manipulated during the design process [22].

Chen et al. employed a topology optimization strategy to design and fabricate gradient NiTi lattice structures [23,24]. Their findings demonstrated the suitability of these structures for energy absorption applications while retaining their shape memory performance. The lattice structure offers the advantage of a larger displacement recovery interval and a smaller accumulative irrecoverable strain. Yan et al. also demonstrated the recoverable strain and energy dissipation capabilities of NiTi lattice structures [25]. They reported that the sample density and cell architecture directly influence the superelasticity and effective transformation stress of the lattices. Notably, their research revealed stable cyclic behavior with 2.8 % of reversible strain achieved through cyclic compression tests conducted below the plastic deformation threshold.

This study is dedicated to the investigation of the functional performance of NiTi architected metastructures fabricated using the LPBF process. These metastructures are inspired by wavy tetra-achiral lattices as introduced by [26]. These lattice designs, along with their tetra-chiral counterparts, exhibit auxetic behavior [27,28]. The distinctive characteristics of these structures make them particularly well-suited for structural applications, especially in energy absorption domains [29–31]. Employing a comprehensive range of microstructural and mechanical characterization techniques, this research aims to comprehensively explore the thermo-mechanical performance of these NiTi metastructures

2. Experimental and numerical methods

2.1. Metastructure design

In this study, the NiTi samples are configured as wavy tetra-achiral lattices, inspired by [26]. These lattices, alongside their tetra-chiral analogs, are associated with isogonal tilings IG62 and IG63, as delineated by Grünbaum and Shephard [32]. Owing to the intrinsic symmetry of tetra-achiral lattices, they lack the axial-shear coupling effect, resulting in enhanced stability under uniaxial compression, in contrast to their tetra-chiral counterparts [26]. The shape of the tetra-achiral lattice aligns with the third resonant mode of a square lattice when analyzed through eigenmode examination. The parameters established by [27] were used as the basis for these structures, leading to their auxetic behavior with in-plane Poisson's ratios of −0.3 along two primary structural directions, behaving similarly to a planar orthotropic

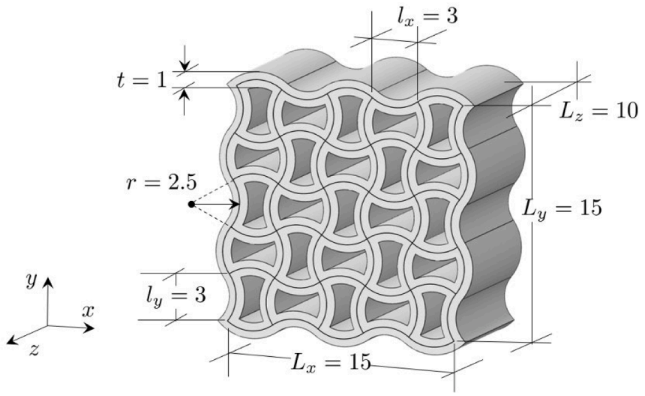

Fig. 1. The geometry of the CAD model for the 3D-printed structure. All specified dimensions are in millimeters. While Lx and Ly both measure 15 mm, accounting for the introduced undulation, the wall thickness results in the structure's outer dimensions being 17 × 17 mm.

Table 1
List of the adopted process parameters used for the printing of the NiTi samples.

Parameters	Value
Power	150 W
Exposure time	75 µs
Scanning strategy	Meander
Atmosphere	Argon
Layer thickness	30 µm
Hatch distance	50 µm
Point distance	120 µm
Laser spot size	65 µm
Platform temperature	30 °C
Platform material	NiTi
Tilting angle	67°
Oxygen level	< 20 ppm

lamina. This behavior mirrors the sinusoidal patterns outlined in Dolla model [33]. Zhang et al. further explored deformation-dependent Poisson's ratios of slotted assemblies of these lattices, modeling the waviness characterized as a sequence of circular arcs with consistent radii and alternating orientations [34]. In scenarios devoid of undulations—where the arc radius approaches infinity—the lattice converges to a conventional square lattice design. Contrasting traditional methods like slotting and stamping, 3D printing technology is employed for fabricating these structures, emulating the absorption efficiency [29]. This necessitates the creation of precise CAD models to accurately direct material deposition in the additive manufacturing phase.

Fig. 1 illustrates the design dimensions. Importantly, this model evolves from an undulated square lattice, preserving the foundational lattice dimensions at lx = ly = 3 mm as the lattice spacing. Following the methodology in [29], we adopted a 5 × 5 2D layout, resulting in an edge-centered structural dimension of Lx = Ly = 15 mm. Considering the introduced undulation and the wall thickness, the outer dimensions of the structure are 17 × 17 mm. Undulations are achieved by transforming square edges into a three-point arc: the arc's endpoints are defined by the square lattice's corners, while the third point is determined by offsetting the edge center in the pertinent direction by 0.5 mm. Consequently, given the parameters used, an arc radius of 2.5 mm is formed. This central undulated pattern is then thickened and extruded in the z-direction to finalize the design. The resulting watertight solid model is then transitioned into an STL model, readying it for 3D printing.

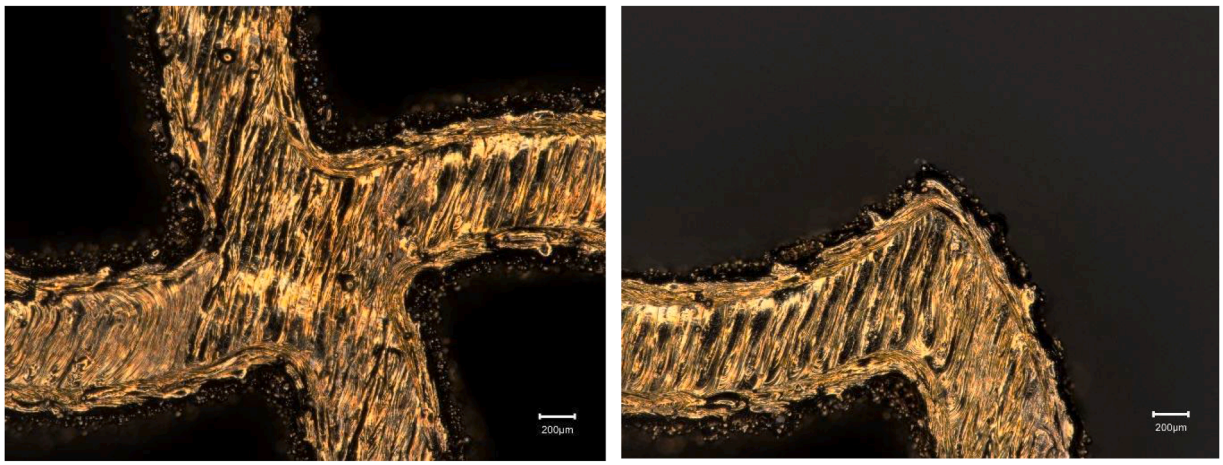

Fig. 2. The optical microscopy images of the NiTi lattices show the quality of the sample fabrication by the LPBF technique on the node (a) and on the edge (b).

2.2. Material and fabrication

NiTi samples were produced utilizing an LPBF system (Renishaw, AM400, UK) employing Ni56Ti46 (wt.%) spherical powder (Nanoval, Germany), having a mesh distribution from 16 µm to 63 µm. The LPBF process parameters outlined in Table 1 were chosen for the fabrication of the NiTi architected structures. The adopted LPBF system was equipped with a pulsed wave laser, and the pulse duration, rather than scanning speed, was utilized to define the appropriate process conditions for achieving the desired NiTi properties [19,35]. The samples were extracted from the platform using a wire electrical discharge cutting machine. To enhance the functional characteristics of the printed specimens, we applied a specific low-temperature heat treatment process. This process primarily aims to release the residual stresses induced by the LPBF process. As a result, the as-built samples underwent annealing at 500 °C for 5 min, followed by water quenching.

2.3. 2D and 3D visual characterization

Optical microscopy images were captured using a Digital Microscope (Keyence, VHX-7000 N, Belgium) for surface investigation of the NiTi lattice samples. A selected sample was subjected to X-ray micro–Computed Tomography (µ-CT) for detailed qualification. The µ-CT was performed using GE equipment (model V, TOMEX), featuring a screen DXR-250 with a pixel size of 2000 × 2000 | 200 µm. The acquisition parameters were set as follows: power=13 W, spatial resolution= 14 µm, and a total of 3000 images were acquired for the examination. The obtained tomography datasets were reconstructed using Dragonfly software (Comet Technologies Canada Inc), and the 3D distribution of deformation or damage in the samples was determined using Dragonfly's segmentation toolkit.

2.4. Microstructural characterization

The martensitic transformation temperatures were detected through differential scanning calorimetry (DSC, model Q25 from TA Instrument, USA), carried out with a heating/cooling scan rate of 10 °C/min, within a temperature range from −100 °C up to 100 °C. Initial NiTi powder, as built and heat treated samples were analyzed through DSC.

Diffraction data (CuKα, λ=1.5418 Å) were collected on a θ:θ vertical scan P analytical X'Pert PRO diffractometer, equipped with parallel (Soller) slits – 0.04 rad – and a real-time multiple strip detector. The generator was operated at 40 kV and 30 mA; slits were used with a divergence of 0.5° The scans were performed in the 10–120° 2θ range at 25 °C. Phase identification was carried out on the heat treated NiTi sample.

Scanning electron microscopy (SEM) was applied for additional examination, employing a Thermo Fisher (Model Phenom XL) and JEOL (Model JSM-7200F) equipped with EDS and electron backscatter diffraction (EBSD) detectors to thoroughly analyze and characterize the microstructure. Image acquisition was conducted using a back-scattered electron (BSE) detector to offer a comprehensive depiction of various

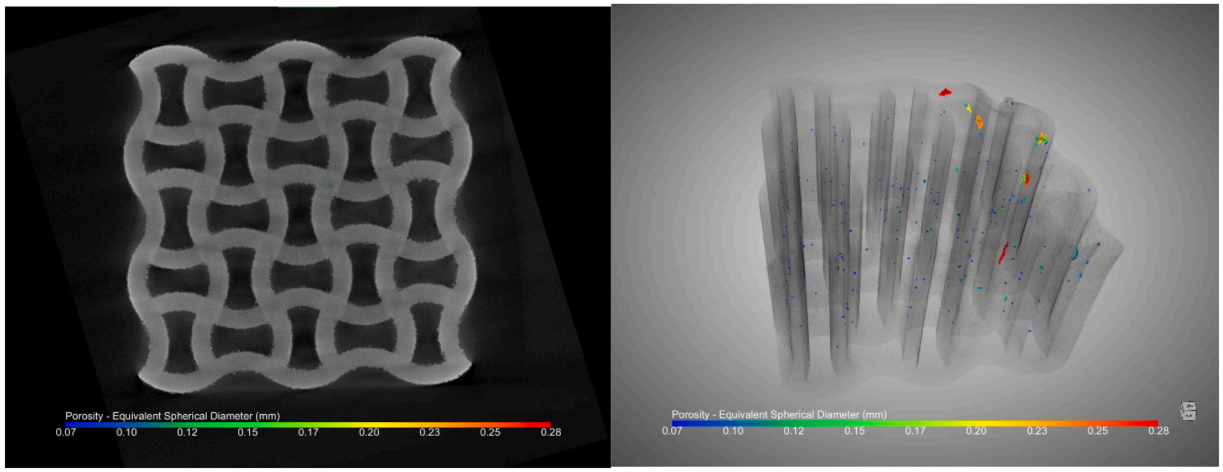

Fig. 3. Micro-CT analysis of the built NiTi architecture sample: xy view (a) and 3D visualization (b).

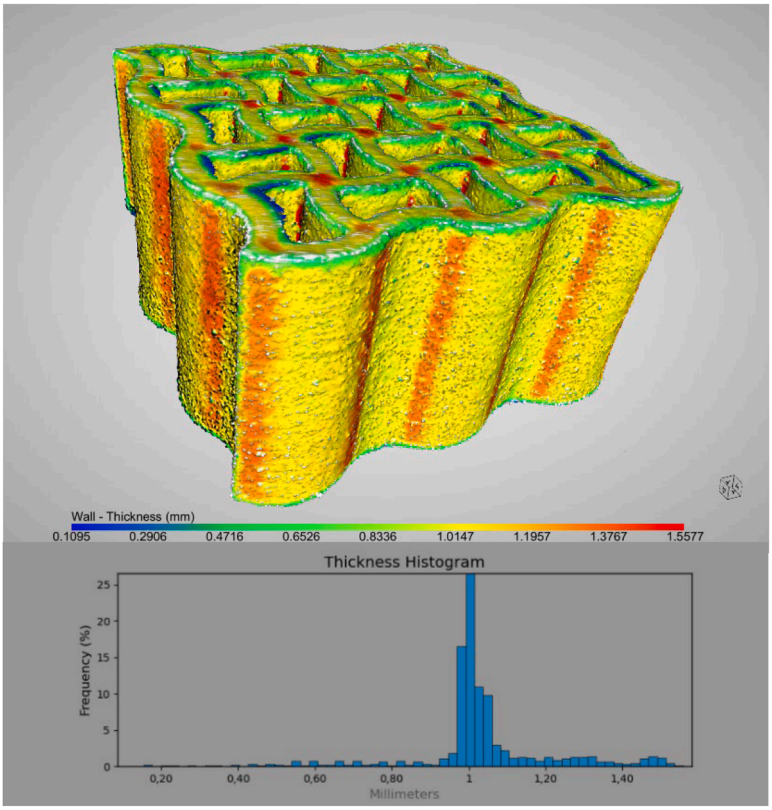

Fig. 4. The trend of the wall thickness of the sample with its statistical analysis.

phases present in the microstructure. To enhance image quality and mitigate charging issues during EBSD imaging, specific samples were embedded in conductive epoxy.

2.5. Mechanical characterization

The mechanical behavior of the NiTi architected structures was investigated through a cyclic compression test, conducted with 10 cycles of loading and unloading to ensure stable mechanical responses for each sample. The tests were performed at room temperature, 25 °C, (using a tensile test machine (Zwick, model Z100, Germany) equipped with a 100 kN load cell. A constant speed of 0.5 mm/min was maintained for all tests at three levels of force (4–8–12 kN), and each test was repeated three times to ensure accuracy and reliability.

3. Results and discussion

3.1. Visual investigation of NiTi structures

The NiTi structures were successfully printed following the experimental plan outlined in the previous section. As depicted in Fig. 2, the printed NiTi lattice exhibits a defect-free surface with no discernible cracks. The scanning strategy employed during printing, comprising meander patterns consisting of contour and hatch paths, is visible on the

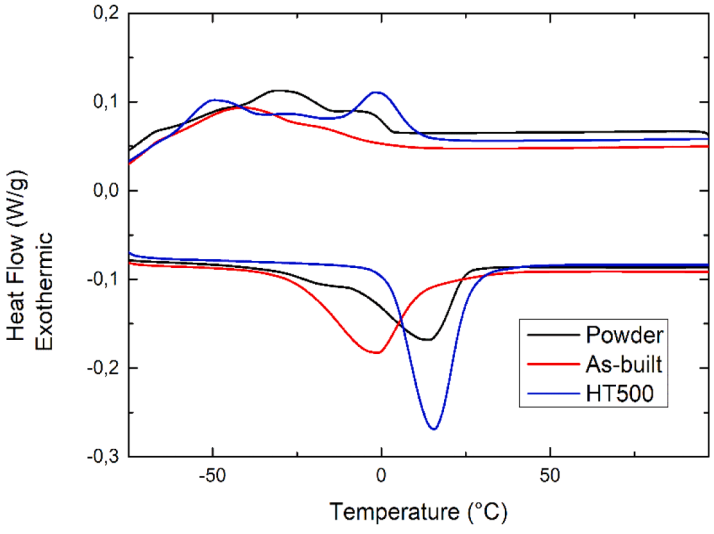

Fig. 5. DSC scans of the initial powder, as built and heat-treated NiTi samples.

Table 2
Transformation Temperatures (TT) of the initial powder, as built and heat-treated NiTi samples. All temperature units are °C.

TT	As	Ap	Af	Rs	Rp	Rf	Ms	Mp	Mf
Powder	−32.5	14	25	3	–	–	–	−30.8	−58
As-built	−25.7	−1.5	17	1	–	–	–	−40.7	−58.5
HT500	2.5	15.5	28	10.5	0.5	−10.7	−37	−50	−60

upper surfaces. The choice of the meander strategy, splitted in hatch and contour, depends on the significant thickness of the architected structure. Previous works were carried out on the printing of NiTi thinner lattice samples, requiring the adjustment of the principal process parameters for implementing a different scanning strategy, namely lattice [19]. Additionally, linear laser scans were used in the central part of the samples, while the border was created using concentric lines.

To evaluate the inner quality of the fabricated structures, a μ-CT scan was performed. The 3D reconstruction in Fig. 3 illustrates the defects' size through a color scale representation. Notably, the nodes of the lattice structure exhibit relatively more defects, with an average size of approximately 100 μm. Also visible are cracks due to the compression testing. Despite the presence of some defects, the volume fraction was measured as 0.07% and this is well within the normal range for an additively manufactured material.

From the μ-CT scans, a wall thickness evaluation could be made. Fig. 4 shows that the wall thickness ranged mainly around 1 mm (shown in yellow) with some thicker regions at the junctions (shown in red). The statistical thickness distribution is included.

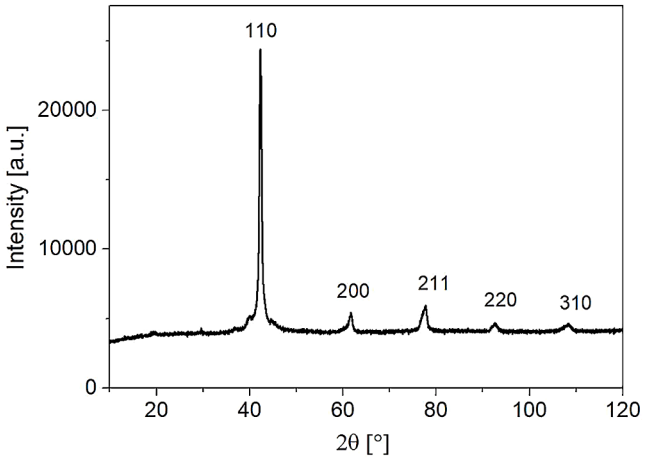

Fig. 6. XRD diffractogram of the heat-treated NiTi sample.

3.2. Microstructural analysis of NiTi structures

The microstructure of the NiTi samples was analyzed through DSC, XRD, and EBSD tests to obtain a complete overview in terms of transformation temperatures of the martensitic transformation, phase identification, and distribution inside the architectural samples.

Initially, the transformation temperatures (TTs) of the initial powder, as-built, and heat-treated samples were measured via DSC. Due to the significant sensitivity of the performances in NiTi SMAs with respect to the chemical composition, it was decided to proceed with a comparative analysis of the TTs from the feedstock material through the LPBF process to the post-treated sample. Further microstructural investigation would focus only on the heat-treated samples.

Fig. 5 presents the DSC test results for the initial NiTi powder, as-built, and heat-treated architected structures. The NiTi powder exhibited a multistage martensitic transformation (MT) upon heating and cooling due to compositional inhomogeneities and residual stresses arising from the gas atomization process [36]. In contrast, the as-built structure displayed a single-stage MT upon heating and a double-stage MT upon cooling, with the two peaks largely overlapping each other, resulting in TT values shifting to lower values. The heat treatment conducted at 500 °C for 5 min (indicated as HT 500) promoted a sharper peak upon heating, indicating the martensite-to-austenite transformation. Additionally, two well-defined peaks were observed during cooling. The first peak corresponded to the transformation from austenite to R-phase, distinguished by limited thermal hysteresis between the peaks upon heating and cooling. The second peak was related to the phase transformation from R-phase to martensite.

Table 2 presents the values of TTs, obtained from the DSC scans shown in Fig. 5. This includes the evaluation of austenite start (As), peak (Ap), and finish (Af), R-phase start (Rs), peak (Rp), and finish (Rf), as well as martensite start (Ms), peak (Mp), and finish (Mf) temperatures, respectively.

In conclusion, the NiTi powder shows wide and partially overlapped peaks of the MT; the corresponding values of TTs confirmed a complete phase transformation in austenite at room temperature, promoting a superelastic behavior. The TTs of the as-built structure, ranged in a similar temperature interval of the power, meaning no significant Ni loss was carried out during the LPBF process.

Fig. 6 shows the XRD spectrum that was carried out on the heat-treated sample at room temperature. Austenite (cubic structure, B2) was predominantly detected in the NiTi sample, consistent with the Austenite Finish (Af) temperature measured from the DSC scans. The sample exhibited a preferential crystallographic orientation, influenced by the rapid laser motion on the powder bed and the subsequent rapid solidification. The most intense diffraction reflection was associated with the (110) peak. Epitaxial growth and columnar grain growth controlled the solidification, attributed to the very high cooling rates characteristic of LPBF.

Additionally, minor peaks associated with the B19′ phase (martensite) were observed. These minor peaks were expected, given that the patterns were collected at room temperature, very close to Af. For a more in-depth understanding of the microstructure, EBSD analysis was conducted.

The EBSD analysis provides a comprehensive insight into the grain formation of the 3D printed samples across various sections of the structure. Fig. 7 illustrates the outcomes of the EBSD test conducted on the XZ section of the sample. Indexing is carried out based on the body-centered cubic austenite. Consequently, the orientation image micrographs (OIM) are computed for the normal direction of the section, along with the inverse pole figures (IPF) in the Z, Y, and X directions.

As depicted, there are non-indexed areas represented in black, suggesting a potential association with localized martensite regions, as reported in other work in the literature [17]. However, most of the analyzed surfaces exhibited the presence of austenite, which is in good agreement with the XRD (Fig. 6) and DSC (Fig. 5) analyses. Similar results were achieved in the literature [37,38]. The results further reveal a lack of uniform texture, with the latter manifesting as a more reddish center and displaying random colors in the OIM. The specimen exhibited elongated grains in the building direction (see Fig. 7), while the shape of the typical liquid pools is not detectable. On the contrary, columnar grains can be observed in Fig. 7, growing orthogonally to the platform, as confirmed by other works in the literature [35].

Fig. 8 presents the results of the EBSD analysis conducted on the XY section of the NiTi samples. In these images, epitaxial grains with dimensions significantly smaller than those in the XZ view (refer to Fig. 7)

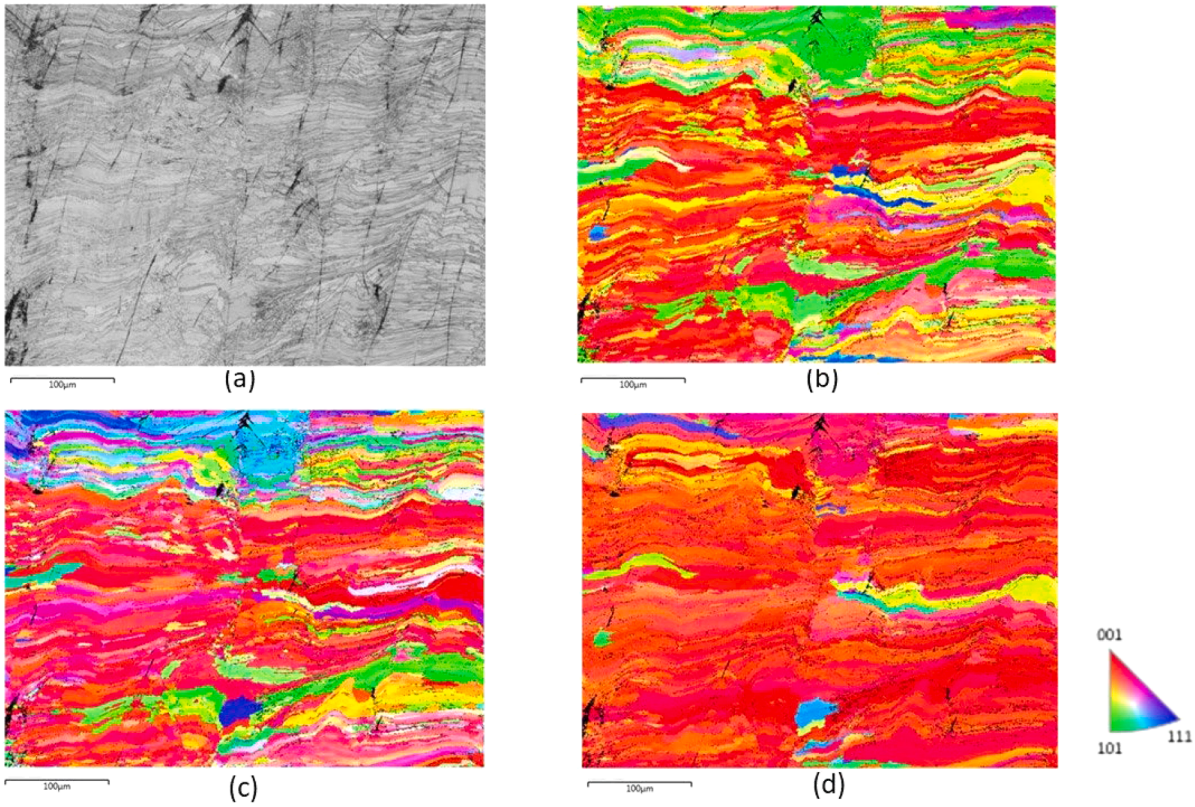

Fig. 7. EBSD analysis of the XZ section in the NiTi structure, depicted using orientation image micrographs (OIM). The visuals correspond to (a) Band Contrast (BC) and (b-d) inverse pole figures (IPF) in the Z, Y, and X directions, respectively.

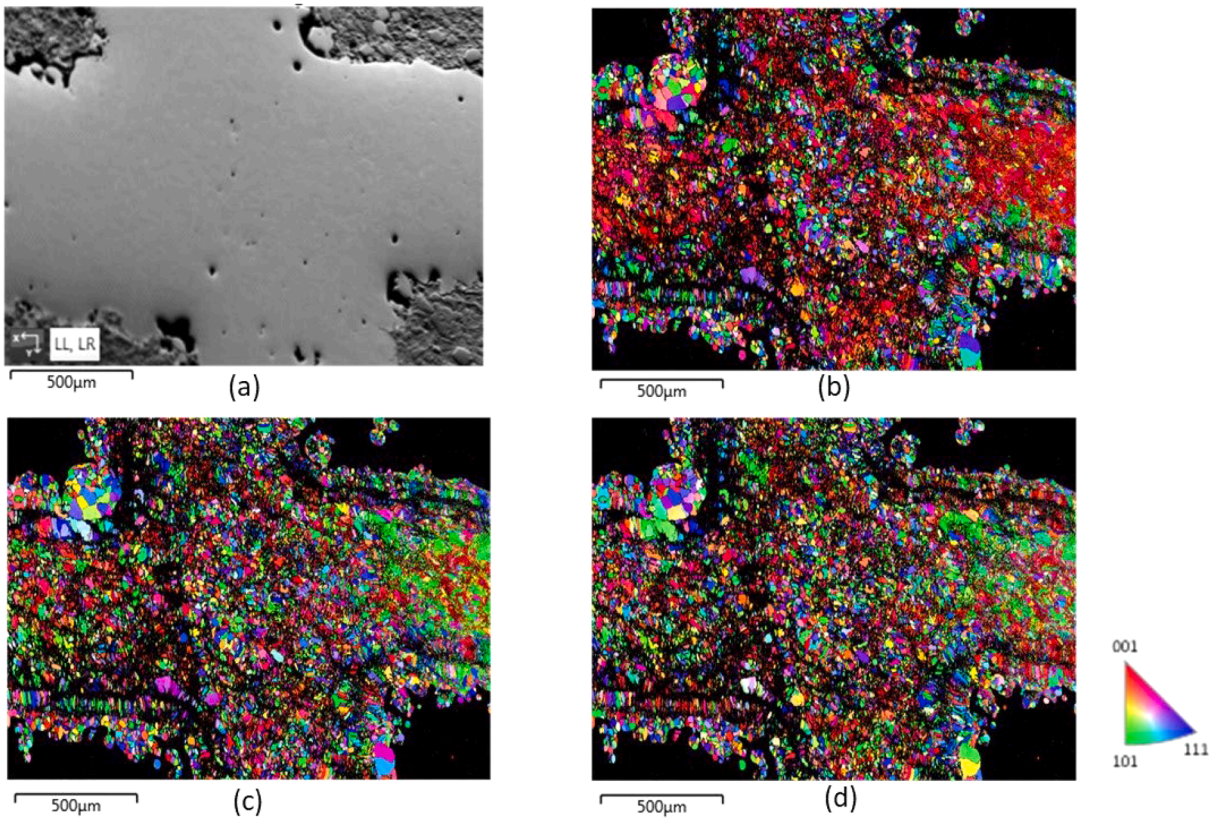

Fig. 8. EBSD findings on the XY section of the NiTi structure, illustrated through orientation image micrographs (OIM). The images correspond to (a) Band Contrast (BC) and (b-d) inverse pole figures (IPF) in the Z, Y, and X directions, respectively.

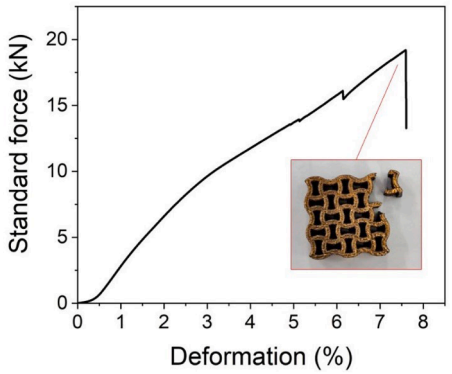

Fig. 9. The result of fracture compression test for a NiTi re-entrant auxetic structure.

were observed. This observation suggests the presence of a notable anisotropic microstructure.

Notably, it highlights a junction on the cellular face where four struts converge at a single point. Similar to the previous picture, the non-indexed regions align with martensite areas, potentially indicative of the presence of stress-induced martensite (SIM). This occurrence may be attributed to stress concentration regions between the struts and nodes. Similar results were also achieved in other works in literature [17]. It can be also noticed that finer microstructure can be seen in the center of the node, while the border of the lattices exhibited slightly larger grains. This may be due to the adopted scanning strategy (meander), in which the contour and the hatch were carried out with different process parameters.

3.3. Mechanical performance of NiTi structures

The compression test was also performed to assess the mechanical strength of the fabricated NiTi lattices at room temperature and determine the point of complete fracture. As shown in Fig. 9, the initial crack initiation occurred at a force of 16.1 kN; however, the complete fracture of the structure was observed at a higher compression force of 19.1 kN, with a corresponding deformation of approximately 7.6 %. The fracture is attributed to stress concentration in the corner of the sample with sharp angles, leading to the failure of the entire sample.

The results from the cyclic compression test demonstrated that the NiTi architected structures displayed stable superelastic responses across all three loading forces (4 kN, 8 kN, and 12 kN). As shown in Fig. 10, except for the first few cycles, the samples maintained their mechanical integrity and superelastic behavior throughout multiple cycles of loading and unloading.

Fig. 11 illustrates the total displacement and recoverable deformations of the NiTi lattice samples subjected to compression tests at 4 kN, 8 kN, and 12 kN. As anticipated, an increase in the applied force, ranging from 4 kN to 12 kN, results in a notable growth in the total displacement by the end of the final loading cycle, measuring 0.4507 mm, 0.5004 mm, and 0.7658 mm respectively. This trend is also observed in the recoverable deformation values, calculated from the unloading displacement of the 10th cycle, revealing values of 0.2572 mm, 0.4081 mm, and 0.6499 mm for the 4 kN, 8 kN, and 12 kN compression tests, respectively. These findings emphasize the structures' capacity to endure repetitive stress and effectively revert to their initial shape, thus making them well-suited for applications demanding reliable and recoverable mechanical responses.

Eq. (1) gives the total dissipated energy for a cyclic force-displacement curve. To this end, the energy associated with the unloading phase, i.e., energy release, is subtracted from the energy associated with the loading phase, i.e., energy input. The total energy dissipation for each successive loading cycle is depicted for the 4 kN, 8 kN, and 12 kN compression tests in Fig. 12. To ascertain the specific dissipation energy, this total value is normalized by the mass of the corresponding lattice.

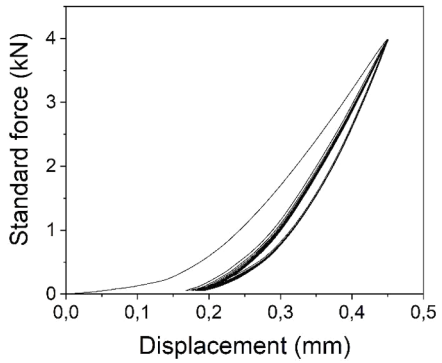

(a)

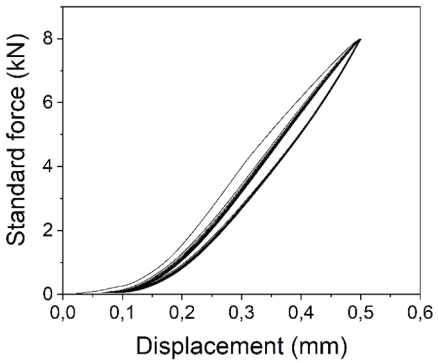

(b)

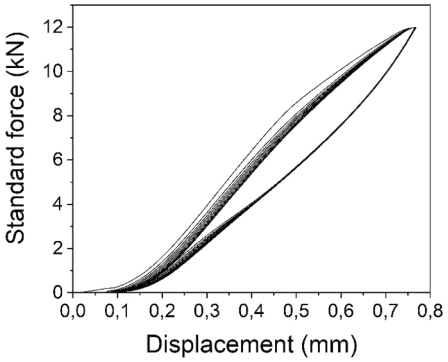

(c)

Fig. 10. The result of the cyclic compression test with a maximum force of (a) 4 kN, (b) 8 kN, and (c) 12 kN after 10 cycles.

$$E_{Disspiated} = \int_{loading} Fdu - \int_{unloading} Fdu \quad (1)$$

The respective lattice masses for compression tests conducted at 4 kN, 8 kN, and 12 kN are 9.327 gs, 9.308 gs, and 9.203 gs. Notably, the initial observations indicate that the obtained results remain stable beyond the initial cycles, persisting throughout the subsequent repetitions up to the 10th cycle. Furthermore, the specific energy dissipation rate can be significantly augmented through an increment in compression force. This augmentation is evidenced by the obtained saturated

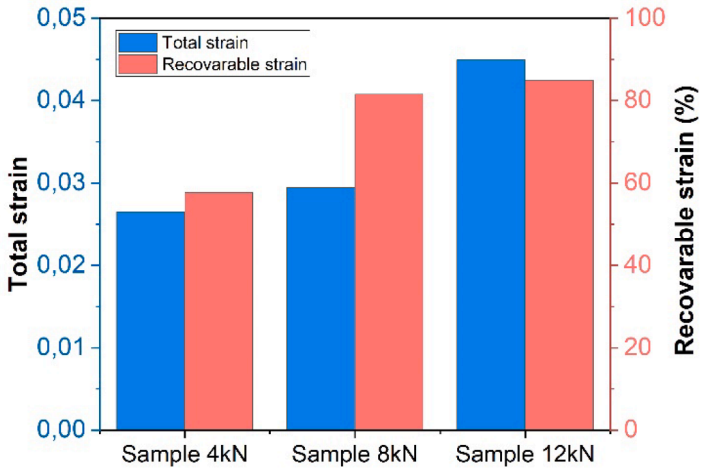

Fig. 11. Summary of compression testing results, showing the total displacement and the recoverable deformation ratio of the NiTi architected structures when compressed to 4 kN, 8 kN, and 12 kN.

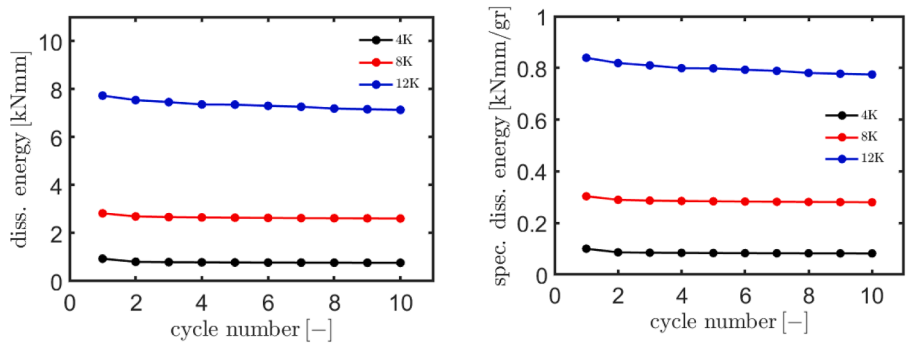

Fig. 12. Dissipated energy and specific dissipation energy values for the NiTi lattice samples were compressed to 4 kN, 8 kN, and 12 kN.

specific energy dissipation values of 0.0821 kN.mm/gr, 0.2802 kN.mm/gr, and 0.7747 kN.mm/gr for the respective loads of 4 kN, 8 kN, and 12 kN.

4. Conclusion

This study investigated the mechanical performance of 3D printed NiTi architected metamaterials. The fabricated samples showcased a remarkable superelastic response emphasizing their potential for diverse and adaptable applications. Moreover, these samples displayed an excellent capacity for energy dissipation and damping behavior, underscoring their efficiency in dissipating mechanical energy. The outcomes of this research are summarized as follows:

- The designed auxetic meta-structures were successfully fabricated using an LPBF printing setup and tested using a wide range of characterization methods. The use of μ-CT scanning allowed us to evaluate the relative density of the lattice structures, which was found to be as high as 99.85 %, signifying excellent overall structural integrity.
- Low-temperature heat treatment, carried out at 500 °C for 5 min, was successfully performed to promote the superelastic properties of the 3D printed NiTi samples. The results showed that the martensitic transformation was set in a temperature range suitable to obtain the austenitic phase.
- The fabricated NiTi metamaterials demonstrated significant recoverable deformation strains ranging from 1.5 to 3.8 %, achieved under an applied force of up to 12 kN. This underscores the capability of this design to enhance the functional performance and deformability of the structure, making it highly suitable for versatile and adaptive applications.

The combination of superelasticity, high deformation capacity, and efficient energy dissipation showcased in this study holds significant implications for various engineering fields, such as aerospace, robotics, and medical devices. These findings provide a solid foundation for further advancements in the design and optimization of 3D printed NiTi architected metamaterials, opening new avenues for materials engineering and enhanced performance in engineered systems.

CRediT authorship contribution statement

C.A. Biffi: Writing – review & editing, Resources, Investigation, Formal analysis. **C. Soyarslan:** Writing – review & editing, Software, Formal analysis, Conceptualization. **J. Fiocchi:** Investigation, Formal analysis. **C. Bregoli:** Investigation, Formal analysis. **A. du Plessis:** Writing – review & editing, Investigation, Formal analysis. **A. Tuissi:** Visualization, Investigation. **M. Mehrpouya:** Writing – original draft, Supervision, Methodology, Investigation, Formal analysis, Conceptualization.

Declaration of competing interest

The authors declare the following financial interests/personal

relationships which may be considered as potential competing interests: One of the authors of this article is part of the Editorial Board of the journal. To avoid potential conflicts of interest, the responsibility for the editorial and peer-review process of this article lies with the journal's other editors. Furthermore, the authors of this article were removed from the peer review process and had no and will not have any access to confidential information related to the editorial process of this article.

Data availability

Data will be made available on request.

Acknowledgements

The authors express their gratitude to Nicola Bennato for his support in the 3D printing process. Also, we would like to appreciate the support of Mr. Nick Helthuis and Mr. Bert Vos for their valuable assistance in setting up the microstructure and mechanical testing procedures.

References

[1] M. Mehrpouya, H.C. Bidsorkhi, MEMS Applications of NiTi Based Shape Memory Alloys: a Review, Micro Nanosyst 8 (2) (2016) 79–91.
[2] Elahinia, M., Shape Memory Alloy Actuators: Design, Fabrication and Experimental Evaluation. 2015, John Wiley & Sons.
[3] Mehrpouya, M., et al., Laser Welding of Nickel-Titanium (NiTi) Shape Memory alloys, in Advanced Welding and Deforming. 2021, Elsevier. p. 203–230.
[4] M. Köhl, et al., Characterization of porous, net-shaped NiTi alloy regarding its damping and energy-absorbing capacity, Mater. Sci. Eng.: A 528 (6) (2011) 2454–2462.
[5] S. Saedi, et al., Energy Damping in Shape Memory Alloys: a Review, J. Alloys Compd. (2023) 170286.
[6] M. Benedetti, et al., Architected cellular materials: a review on their mechanical properties towards fatigue-tolerant design and fabrication, Mater. Sci. Eng.: R: Rep. 144 (2021) 100606.
[7] D. Gu, et al., Additively manufacturing-enabled hierarchical NiTi-based shape memory alloys with high strength and toughness, Virtual Phys. Prototyp. 16 (sup1) (2021) S19–S38.
[8] L. Riva, P.S. Ginestra, E. Ceretti, Mechanical characterization and properties of laser-based powder bed–fused lattice structures: a review, Int.. J. Adv. Manuf. Technol. 113 (2021) 649–671.
[9] M.K. Ravari, et al., On the effects of geometry, defects, and material asymmetry on the mechanical response of shape memory alloy cellular lattice structures, Smart Mater. Struct. 25 (2) (2016) 025008.
[10] S. Afkhami, et al., Mechanical performance and design optimisation of metal honeycombs fabricated by laser powder bed fusion, Thin-Walled Struct. 180 (2022) 109864.
[11] C.W. Isaac, F. Duddeck, Recent progress in 4D printed energy-absorbing metamaterials and structures, Virtual Phys. Prototyp. 18 (1) (2023) e2197436.
[12] A. Jafarabadi, et al., 4D printing of recoverable buckling-induced architected iron-based shape memory alloys, Mater. Des. 233 (2023) 112216.
[13] A. du Plessis, et al., Properties and applications of additively manufactured metallic cellular materials: a review, Prog Mater Sci (2021) 100918.
[14] F. Yazdandoost, et al., Energy dissipation of shock-generated stress waves through phase transformation and plastic deformation in NiTi alloys, Mech. Mater. 137 (2019) 103090.
[15] D. Kim, et al., 3D and 4D Printing of Complex Structures of Fe Mn Si-Based Shape Memory Alloy Using Laser Powder Bed Fusion, Adv. Mater Interfaces 9 (13) (2022) 2200171.
[16] R. Xi, et al., Effect of Fe addition on the microstructure, transformation behaviour and superelasticity of NiTi alloys fabricated by laser powder bed fusion, Virtual Phys. Prototyp. 18 (1) (2023) e2126376.
[17] S. Khademzadeh, Precision additive manufacturing of NiTi shape memory parts using micro-laser powder bed fusion, Progr. Addit. Manuf. (2021) 1–14.
[18] T. Gustmann, et al., Properties of a superelastic NiTi shape memory alloy using laser powder bed fusion and adaptive scanning strategies, Progre. Addit. Manuf. 5 (2020) 11–18.
[19] C.A. Biffi, et al., Microstructural and mechanical response of NiTi lattice 3D structure produced by selective laser melting, Metals (Basel) 10 (6) (2020) 814.
[20] S. Bernard, et al., Compression fatigue behavior of laser processed porous NiTi alloy, J. Mech. Behav. Biomed. Mater. 13 (2012) 62–68.
[21] M.T. Andani, et al., Mechanical and shape memory properties of porous Ni50. 1Ti49. 9 alloys manufactured by selective laser melting, J. Mech. Behav. Biomed. Mater. 68 (2017) 224–231.
[22] S. Dadbakhsh, et al., Laser additive manufacturing of bulk and porous shape-memory NiTi alloys: from processes to potential biomedical applications, MRS Bulletin 41 (10) (2016) 765–774.
[23] W. Chen, et al., Compressive mechanical properties and shape memory effect of NiTi gradient lattice structures fabricated by laser powder bed fusion, Int. J. Extreme Manuf. 4 (4) (2022) 045002.
[24] J. Sun, et al., Laser powder bed fusion of diatom frustule inspired bionic NiTi lattice structures: compressive behavior and shape memory effect, Smart Mater. Struct. 31 (7) (2022) 074003.
[25] Z. Yan, et al., Superelastic response and damping behavior of additively manufactured Nitinol architectured materials, Addit. Manuf. 68 (2023) 103505.
[26] Z. Yuan, Z. Cui, J. Ju, Micropolar homogenization of wavy tetra-chiral and tetra-achiral lattices to identify axial–shear coupling and directional negative Poisson's ratio, Mater Des. 201 (2021) 109483.
[27] C. Körner, Y. Liebold-Ribeiro, A systematic approach to identify cellular auxetic materials, Smart Mater. Struct. 24 (2) (2014) 025013.
[28] C.A. Biffi, et al., Functional performance of NiTi shape memory architected structures produced by laser powder bed fusion (LPBF), Trans. Addit. Manuf. Meets Med. 5 (S1) (2023) 821.
[29] A. Mauko, et al., Dynamic deformation behaviour of chiral auxetic lattices at low and high strain-rates, Metals (Basel) 11 (1) (2020) 52.
[30] X.-c. Zhang, et al., Dynamic crushing responses of bio-inspired re-entrant auxetic honeycombs under in-plane impact loading, Mater. Today Commun. 23 (2020) 100918.
[31] Y. Zhang, et al., Static and dynamic properties of a perforated metallic auxetic metamaterial with tunable stiffness and energy absorption, Int. J. Impact Eng. 164 (2022) 104193.
[32] B. Grünbaum, G.C. Shephard, Tilings and Patterns, Courier Dover Publications, 1987.
[33] Dolla, W.J.S., B.A. Fricke, and B.R. Becker, Structural and drug diffusion models of conventional and auxetic drug-eluting stents. 2007.
[34] Y. Zhang, et al., In-plane compressive properties of assembled auxetic chiral honeycomb composed of slotted wave plate, Mater. Des. 221 (2022) 110956.
[35] C.A. Biffi, et al., Selective laser melting of NiTi shape memory alloy: processability, microstructure, and superelasticity, Shape Memory Superelastic. 6 (2020) 342–353.